Materials Today Bio 17 (2022) 100493

Contents lists available at ScienceDirect

Materials Today Bio

journal homepage: www.journals.elsevier.com/materials-today-bio

Iron acquisition and mineral transformation by cyanobacteria living in extreme environments

Wei Huang [a,b], Taifeng Wang [a], Cesar Perez-Fernandez [c], Jocelyne DiRuggiero [c], David Kisailus [a,*]

[a] Department of Materials Science and Engineering, University of California Irvine, CA, USA
[b] School of Materials Science and Engineering, Huazhong University of Science and Technology, Wuhan, China
[c] Department of Biology, Johns Hopkins University, Baltimore, MD, USA

ARTICLE INFO

Keywords:
Microorganisms
Biofilm
Magnetite
Extreme environment
Iron acquisition

ABSTRACT

Iron is an essential micronutrient for most living organisms, including cyanobacteria. These microorganisms have been found in Earth's driest polar and non-polar deserts, including the Atacama Desert, Chile. Iron-containing minerals were identified in colonized rock substrates from the Atacama Desert, however, the interactions between microorganisms and iron minerals remain unclear. In the current study, we determined that colonized gypsum rocks collected from the Atacama Desert contained both magnetite and hematite phases. A cyanobacteria isolate was cultured on substrates consisting of gypsum with embedded magnetite nanoparticles. Transmission electron microscopy imaging revealed a significant reduction in the size of magnetite nanoparticles due to their dissolution, which occurred around the microbial biofilms. Concurrently, hematite was detected, likely from the oxidation of the magnetite nanoparticles. Higher cell counts and production of siderophores were observed in cultures with magnetite nanoparticles suggesting that cyanobacteria were actively acquiring iron from the magnetite nanoparticles. Magnetite dissolution and iron acquisition by the cyanobacteria was further confirmed using large bulk magnetite crystals, uncovering a survival strategy of cyanobacteria in these extreme environments.

1. Introduction

Microbial communities inhabit rock substrates (endoliths) as a survival strategy in arid deserts around the world such as the Atacama Desert, Chile [1–3]. Cyanobacteria, a major component of endolithic communities in hyper-arid environments, utilize crystalline water from gypsum rocks as a source of moisture for metabolic activity [4]. In fact, it is these rocks that provide refuge for a variety of microbial taxa that include not only *Cyanobacteria*, but also *Actinobacteria*, *Chloroflexis*, and *Proteobacteria* [5,6]. Beyond water, cyanobacteria also acquire trace elements from their rocky habitat, such as iron, an essential micronutrient for many enzymatic processes and for photosynthesis [7,8].

Although iron is in relatively high abundance in the environment, its accessibility to microorganisms is low because it is found primarily as minimally soluble ferric (Fe^{3+}) ions within oxide minerals such as hematite, magnetite, siderite, etc. [9]. As a result, microorganisms have evolved several iron acquisition pathways including siderophores, heme and transferrin/lactoferrin uptake (i.e., hemophores), and reduction of Fe(III) to Fe(II) with subsequent transport of Fe(II) [8]. Siderophores are of particular interest in extreme environments where heme-producing hosts are lacking; Siderophores are low molecular-weight organic ligands with high affinity and specificity for Fe. Siderophores mobilize Fe by competitive complexation or dissolution of iron-bearing minerals for delivery to cells via specific receptors [10–13]. In the past few years, the uptake and transport pathways of iron by siderophores have been thoroughly investigated in bacteria [14]. However, the pathways by which ferric iron is extracted from minerals at neutral pH in the presence of bacteria and the interactions between bacteria and iron-based mineral surfaces remain unclear [15,16]. Significant progress had been made in understanding how dissimilar iron reducing bacteria (DIRB) such as *Shewanella putrefaciens* can transform magnetite to siderite or vivianite and thus utilized in biogeochemical reactions including redox balance and oxidation of organic carbon [17–20]. In contrast, it was reported that chemolithoautotrophic bacteria form organic carbon compounds by reducing carbon dioxide while oxidizing manganese minerals. In this case, Mn(II) in $MnCO_3$ was oxidized to Mn(IV)O_2 in presence of the microorganisms, in which the inorganic manganese phase serves as an electron donor [15].

---

* Corresponding author.
E-mail address: david.k@uci.edu (D. Kisailus).

https://doi.org/10.1016/j.mtbio.2022.100493
Received 19 August 2022; Received in revised form 26 October 2022; Accepted 10 November 2022

In this work, gypsum was collected from the Atacama Desert to investigate interactions between microbial cells and minerals within the context of iron acquisition. In addition to revealing survival strategies of cyanobacteria in an extreme desert, the modifications of geological minerals and synthetic ceramics by microorganisms could lead to new insights that are important in biomineralization [21–29] as well as biomedical applications such as bioimaging or targeted drug delivery [30–37] and could also provide inspiration for the design and fabrication of functional living materials [38–40]. An engineered living material is a category of smart materials that incorporate living cells within matrices (scaffolds), thus providing active responses to environmental stimuli [41]. Applications of living materials in the biomedical field include wound healing and biosensing, while environmentally friendly building composites have been developed by researchers in civil engineering [42,43]. Beyond this, understanding these organic-mineral interactions could also yield new strategies for the synthesis of new functional materials with novel properties for a broad range of applications [44–50]. The interactions between living cells with the materials matrices (polymers or ceramics) occur in extreme environments, providing crucial information for the extreme biomimetic designs, leading to novel material synthesis and fabrication strategies under extreme biological conditions [51,52].

2. Experiments and methods

2.1. Sample collection and preparation

Gypsum rocks containing microorganisms and iron minerals were collected in the Atacama Desert, Chile as described in Ref. [4]. Particles containing black and orange minerals were picked out from the gypsum rocks acquired in the desert and embedded in epoxy (System 2000, Fibreglast) for further study. Bulk magnetite crystals were purchased from a commercial source (CrystalShopsUSA, NC), also embedded in epoxy, and polished to expose the mineral surfaces for the cyanobacteria culture experiments.

2.2. Optical and scanning electron microscopy

The embedded gypsum and iron oxide rock samples acquired in the previous section were gradually polished using a series of SiC and diamond abrasives down to 50 nm grit. Optical micrographs were taken on the polished surfaces. Both of the original gypsum/iron oxide rock samples collected from the Atacama Desert and synthesized samples tested in the cyanobacteria culture experiments were examined via scanning electron microscopy (Tescan GAIA3 SEM, Czech Republic). All of the samples were sputter coated with a thin layer (~6 nm) of Pt/Pd before SEM examination. Energy dispersive x-ray spectroscopy (EDX) and mapping were performed to study the elemental content and distribution on the samples.

2.3. Synchrotron X-ray fluorescence microscopy and X-ray absorption near edge structure

Synchrotron X-ray fluorescence microprobe measurements on the gypsum rock samples collected from the Atacama Desert were performed at XFM beamline 10.3.2 of the Advanced Light Source (ALS), Lawrence Berkeley National Laboratory (LBNL) Berkeley, CA, USA. All data were recorded with the storage ring operating in top-off mode at 500 mA, 1.9 GeV. Micro-focused X-ray fluorescence (μXRF) mapping and X-ray absorption near-edge structure (μXANES) spectroscopy were performed at room temperature in fluorescence mode using a single element XR-100 FAST C2 silicon drift detector (Amptek). The samples were oriented at 45° to the incident X-ray beam. XRF maps were recorded at 7210 eV (100 eV above the Fe K-edge) using a beam spot size of 2 × 2.5 μm, with 1 × 1 μm or 1.5 × 1.5 μm pixel size and 50 ms dwell time/pixel. Micro-XRF spectra were recorded simultaneously on each pixel of the maps. All maps were then deadtime-corrected, and decontaminated using custom LabVIEW2018 (National Instruments, Austin, TX, USA) software available at the beamline.

Fe K-edge μXANES spectra were recorded on sample regions of interest using a beam spot size of 2 × 2.5 μm followed by least-squares linear combination fitting (LCF) to determine Fe chemical speciation. XANES spectra were recorded by continuously scanning the Si (111) monochromator (Quick XAS mode) in the 7010–7414 eV range, with 0.3 eV steps near the edge (7096–7140 eV). Spectra were calibrated using an Fe foil, with the first derivative set at 7110.75 eV. Spectra were deadtime corrected, deglitched, calibrated, pre-edge background subtracted and post-edge normalized using custom LabVIEW2018 software available at the beamline LC fitting was then performed in the range 7090 to 7365 eV using a large spectral database of Fe standard compounds to identify mineral groups present. The best fit was chosen using a maximum of three components based on the minimum normalized sum-square value $NSS = 100 \times [\sum(\mu_{exp} - \mu_{fit})^2 / \sum(\mu_{exp})^2]$, for which the addition of a spectral component to the fit required a 10% or greater improvement in the NSS value. The uncertainty on the percentages of compounds present is estimated to be ±10%.

2.4. Magnetite nanoparticle synthesis

A bioinspired two-step method was used to synthesize magnetite nanoparticles. First, ferrihydrite as a precursor was obtained by adding a 1 M NaOH solution with an addition rate of 1 mL/min into 50 mL of 30 mM $FeCl_3 \cdot 6H_2O$ solution, until the pH reached 7. This reaction was carried out in a glass beaker with rigorous stirring. A stock solution was prepared from the obtained dispersion by dilution to reach 3 mM Fe(III) concentration. Next, 50 mL of the as-synthesized ferrihydrite suspension was degassed via bubbling with argon gas for at least 30 min. Under constant stirring, 15.9 mg of $FeCl_2 \cdot 4H_2O$ (1.6 mM Fe(II)) was subsequently added, followed by pH adjustment with periodic additions of 1 M NaOH solution (every 5 min) to maintain the pH at 8 for 3 h. The entire beaker reaction system was well sealed with parafilm, leaving one port for constant inert Ar gas flow to avoid oxidation by air. Finally, the black precipitate of magnetite particles was collected, washed with Milli Q water 3 times and dried in the oven overnight at 60 °C. The final magnetite product was further examined with powder X-ray diffraction and transmission electron microscopy.

2.5. Cyanobacteria culture

Magnetite nanoparticles prepared as described above were mixed with an aqueous slurry of gypsum powder and cast in a silicone mold to make magnetite coupons (dimensions of ~5 mm diameter and 2 mm thickness). Pure gypsum coupons were also prepared as controls. In addition, coupons with commercially sourced bulk magnetite crystals embedded in epoxy resin were also prepared. All of the coupons were sterilized under UV for 30 min in a laminar flow hood and then placed aseptically in 96 well plates.

Cultures of the cyanobacterium G-MTQ-3P2 (*Chroococcidiopsis* sp) isolated from colonized gypsum from the Atacama Desert [53], were grown in BG11 medium or iron-depleted BG11 medium at 25 °C under 24 μmoles photons/m^2/s of white light. The iron-depleted BG11 medium was prepared by omitting iron in the medium composition and by treating the medium with Chelex 100 to chelate trace iron, as previously described [54]. 100 μl of cultures were used to inoculate each coupon with 10^6 - 10^7 cells. Controls included cultures without coupon and coupons with sterile BG11 medium. The 96 well-plates were incubated at 25 °C under 24 μmoles photons/m^2/s of white light for 21 days. During that time, BG11 medium or iron-depleted BG11 medium were added periodically to keep a thin liquid layer on top of each coupon. On day 21, coupons were harvested with sterile tweezers, placed in microfuge tubes, flash-frozen with dry ice and stored at −80 °C until further processing.

The frozen samples were further examined via Raman spectroscopy and mapping as well as SEM to study the surface morphology and phase information of the magnetite minerals after the culture experiments.

Cyanobacteria were also grown in liquid cultures (20 mL each) with either BG11 medium, iron-depleted BG11 medium, or iron-depleted BG11 medium supplemented with 2.5 mg of synthetized magnetite nanoparticles. The cultures were inoculated with ~10^6 cells, previously resuspended in iron-depleted BG11 medium, and incubated at 25 °C under 24 μmoles photons/m^2/s of white light for 21 days. On day 21, 1 mL aliquots of each culture were centrifuged at 15,000×g for 10 min at 4 °C, the supernatant was removed, the cell pellets were frozen with dry ice, and stored at −80 °C until further processing for chlorophyll (Chl *a*) measurements.

2.6. Chlorophyll a and siderophore measurements

It was impossible to use microcopy cell count or optical density to evaluate cell abundance in the liquid cultures because of the presence of insoluble nanoparticles and cell aggregates, instead, we used Chl *a* concentration measurements as a proxy, as previously described in Ref. [55]. In brief, pigments were extracted from cells using methanol and their concentrations were measured by spectrophotometry at 665 nm and 720 nm. Chl *a* concentrations were calculated according to the equation: Chl *a* [μg/ml] = 12.9447 ($A_{665} - A_{720}$). Each measurement was carried out in triplicate with 1 mL of culture per measurement.

Siderophore content in the supernatant of liquid cultures was measured with the CAS assay for siderophore detection based on the utilization of chrome azurol S (CAS), as previously described [56]. In brief, cultures were centrifuged at 15,000×g for 10 min at RT; the supernatant was then mixed with the CAS assay solution in a 1:1 ratio and incubated for 4 h at RT followed by absorbance measurements at 630 nm. Zero absorbance was calibrated with a mixture of CAS assay solution and 1.5 mM deferoxamine mesylate (DFOM). Corresponding sterile media were used as reference solutions containing no siderophore. Estimated siderophore concentrations were calculated from standard curves with DFOM and expressed as DFOM equivalents. Each data point was the mean of 3 replicates.

2.7. Raman spectroscopy and mapping

The magnetite and hematite phases in the original rock samples and coupons before and after cell culture experiments were examined via Raman spectroscopy and mapping. A Horiba XploRA PLUS Confocal Raman microscope (Horiba, Japan), equipped with a 785 nm laser, was utilized in the tests. Maps with dimensions of 70 μm × 70 μm and step sizes of 2 μm were acquired. At least 3 maps were taken at different positions for each sample.

2.8. Transmission electron microscopy

The embedded magnetite nanoparticle samples exposed to cyanobacteria cultures were examined via high resolution TEM. Thin films (~70 nm) of the samples for TEM imaging were prepared using an ultramicrotome (RMC MT-X; Boeckeler Instruments). A JEOL JEM 2800 TEM was used at 200 KV for imaging.

3. Results and discussions

3.1. Magnetite and hematite minerals in gypsum from the Atacama Desert

Gypsum rocks collected from the Atacama Desert, Chile (Fig. 1a), harbored black and orange-colored particles most likely due to iron

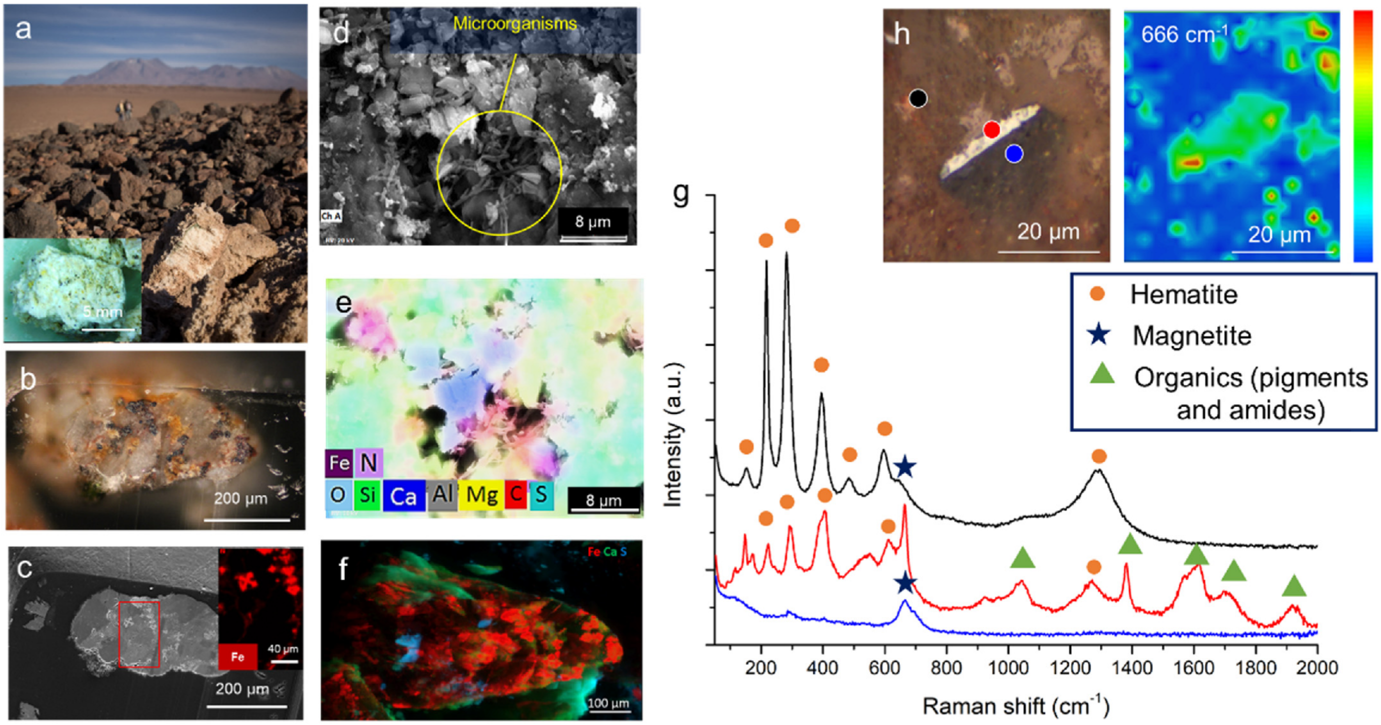

Fig. 1. Iron minerals in gypsum rocks collected from the Atacama Desert. (a) Field photo of the Atacama Desert. Inset photo shows the rocks collected from the desert. (b) Optical microscopy image of black and yellow particles found in gypsum rock, inset of (a). (c) SEM micrograph of the polished surface in (b) and EDS mapping of iron (inset). (d, e) SEM micrograph of inset of (a) showing particles embedded within rock and microbe colonies. The EDS mapping showing distribution of iron (purple) and microorganisms (red and lavender). (f) Synchrotron micro X-ray fluorescence microscopy of the gypsum rock sample in (b). The distribution of iron, calcium and sulfur are shown in red, green and blue, respectively. Pixel size is 1.5 μm × 1.5 μm. (g, h) Raman spectroscopy and mapping of the mineral sample of the inset (a), indicating the existence of magnetite and hematite phases. (For interpretation of the references to colour in this figure legend, the reader is referred to the Web version of this article.)

minerals inclusions (inset, Fig. 1a). The presence of iron in the black particles and its distribution inside the rock were confirmed by optical microscopy and SEM/EDX mapping (Fig. 1c). A closer examination of the sample using scanning electron microscopy (SEM) revealed the presence of filamentous microorganisms within the rocky substrate (Fig. 1d). Based on previous studies of gypsum rocks from several locations of the Atacama Desert [57–59], filamentous microorganisms likely belong to actinobacteria as well as cyanobacteria from the *Nostocales* and *Oscillatoriales* orders. *Chroococcidiopsis*, although non-filamentous, were also a well-represented taxon in the gypsum communities. These cyanobacteria have been found in aggregates around sepiolite minerals where water was available for metabolism [57]. EDX mapping (Fig. 1e of the same area from Fig. 1d) provided the elemental distribution of the rock surface, in which iron (Fe) and the organic content, suggestive of bacterial occurrence, were observed from C, S and N abundances. Based on the color and presence of iron, the observed black particles within the gypsum rocks were likely magnetite. To further confirm this, we obtained elemental distributions and determined mineral groups present at the micron scale using polished flat surfaces of the black particles and synchrotron micro X-ray fluorescence (μXRF) microscopy and X-ray absorption near edge structure (μXANES) spectroscopy. Micro-XRF mapping revealed that iron, calcium, potassium, and sulfur were the major elements detected in the rock, and that iron was found in both ferric and ferrous forms (Fig. 1f and S 1, Table S1). Least-square linear combination fitting of Fe K-edge XANES data (Fig. S2) provided mineral phase information and further indicated the presence of magnetite within the gypsum rocks. Additional analyses of these minerals by powder and wide-angle X-ray diffraction (Figs. S3a and b, respectively) highlighted both magnetite and hematite phases.

Raman spectroscopy and mapping were performed on the rock samples to provide the spatial distribution of magnetite and hematite phases. Both magnetite and hematite phases were confirmed by Raman spectroscopy (Fig. 1g). Raman mapping (Fig. 1h) depicted regions of magnetite within the rock (as selected by highlighting the peak at 666 cm^{-1}, which is the most intense peak of magnetite phase) [60]. Furthermore, the red Raman spectrum in Fig. 1g, which was based on the red spot in Fig. 1h, showed peaks at 1615, 1382, and 1271 cm^{-1} that were assigned to pigments such as xanthophylls, carotenoids, and amide in cyanobacteria [57,61]. The presence of iron-based minerals and biological pigments at the same location in the gypsum samples suggested potential cyanobacteria-mineral interactions for iron acquisition.

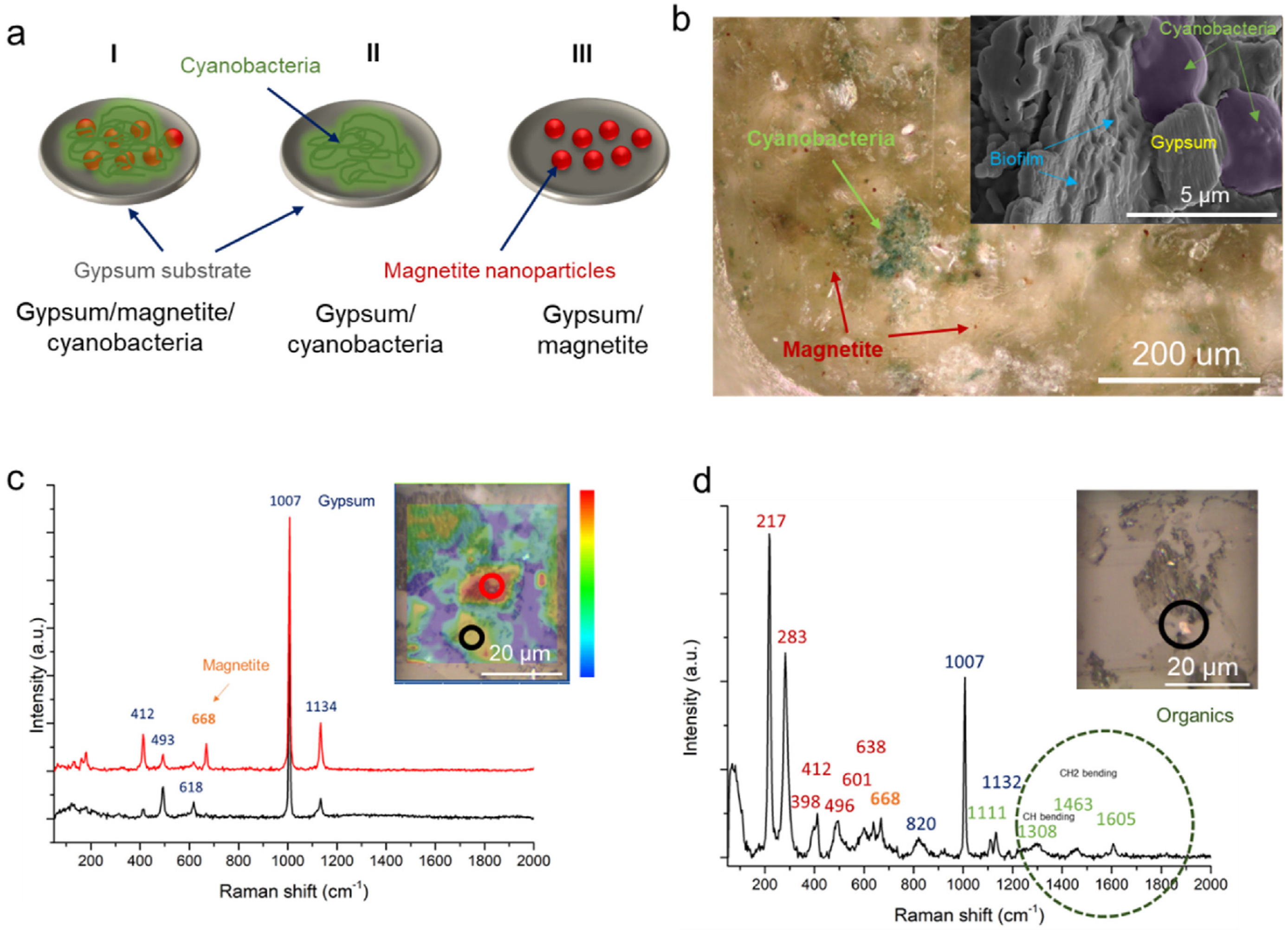

Fig. 2. Cyanobacteria cultures on gypsum substrates with or without magnetite nanoparticles. (a) Three different groups of the culture experiments were conducted: I) Gypsum substrate with embedded magnetite nanoparticles and cultured with cyanobacteria. II) Gypsum substrate without magnetite nanoparticles and cultured with cyanobacteria. III) Gypsum substrate with embedded magnetite nanoparticles without cyanobacteria (negative control). (b) Optical micrograph showing the cyanobacteria and magnetite nanoparticles in the substrate. Inset SEM image shows the cyanobacteria and surrounding biofilm attached to the gypsum substrate. (c) Raman spectroscopy of sample (III). The inset image shows the distribution (red is highest, blue is lowest) of magnetite. (d) Raman spectroscopy of sample (I) from region circled in black (inset). Hematite and magnetite phases, as well as organics are observed. (For interpretation of the references to colour in this figure legend, the reader is referred to the Web version of this article.)

3.2. Interactions between cyanobacteria and magnetite nanoparticles

To understand the interactions between cyanobacteria and iron minerals, *Chroococcidiopsis* sp. G-MTQ-3P2 were cultured with gypsum substrates either with or without embedded synthesized magnetite nanoparticles (Fig. S5). Small changes (even at nanoscale) to the size or phase of these magnetite nanoparticles can be monitored via transmission electron microscopy (TEM). Fig. 2a shows the three groups utilized for the experiments: I) experimental group: cyanobacteria with coupons of gypsum and synthesized magnetite nanoparticles; II) control group: cyanobacteria with coupons of gypsum without synthesized magnetite nanoparticles; III) control group: coupons of gypsum and synthesized magnetite nanoparticles without cyanobacteria. After 21 days of culturing, the surface of sample I demonstrated the presence of green cyanobacteria colonies within a biofilm attached to the substrate (Fig. 2b). To compare the effect of the growing colonies on any phase changes in magnetite, Raman spectroscopy and mapping were performed on samples I and III after the culture experiments. In sample III (control with no cyanobacteria), only magnetite was observed (Fig. 2c), whereas in sample I, both hematite and magnetite phases were present (Fig. 2d).

We further investigated potential size and phase changes of the magnetite nanoparticles during the culture experiments with high resolution transmission electron microscopy (HRTEM) imaging of the nanoparticles in samples I and III. Aggregates of nanoparticles shown within control sample III (i.e., no cyanobacteria, Fig. 3a), with selected area electron diffraction (SAED, inset 3a) and Fast Fourier Transformation (FFT, Fig. 3b), revealed a randomly oriented magnetite phase. The average size of these highly crystalline nanoparticles (Figs. 3c and d) was ~15.8 ± 3.1 nm, which was comparable to the original synthesized nanoparticles that were introduced before the culturing experiments (Fig. S4). Conversely, nanoparticles within aggregates from sample I (containing cyanobacteria) had a significantly smaller size (~7.1 ± 1.1 nm, Fig. 3e) than the initial magnetite nanoparticles introduced before culturing. Phase analysis of these particles using FFT verified the presence of hematite after the culturing with cyanobacteria (Fig. 3f). HRTEM images of the hematite nanoparticles showed both crystalline and amorphous domains (Figs. 3g and h). A close comparison of the magnetite nanoparticle aggregates in Fig. 3a and e revealed the presence of what appeared to be organic biofilms surrounding the hematite nanoparticle aggregates in sample I (Fig. 3e). The organic biofilm was detected in SEM and validated with EDX before TEM sample preparation (Fig. S6). This observation corroborated our Raman spectrum acquired from the same specimen (i.e., Sample I, Fig. 2d). HRTEM images and the FFT pattern suggested the presence of amorphous films (Figs. 3i and j) surrounding hematite-containing nanoparticles; these were likely organic biofilms leading to the dissolution of iron-based mineral

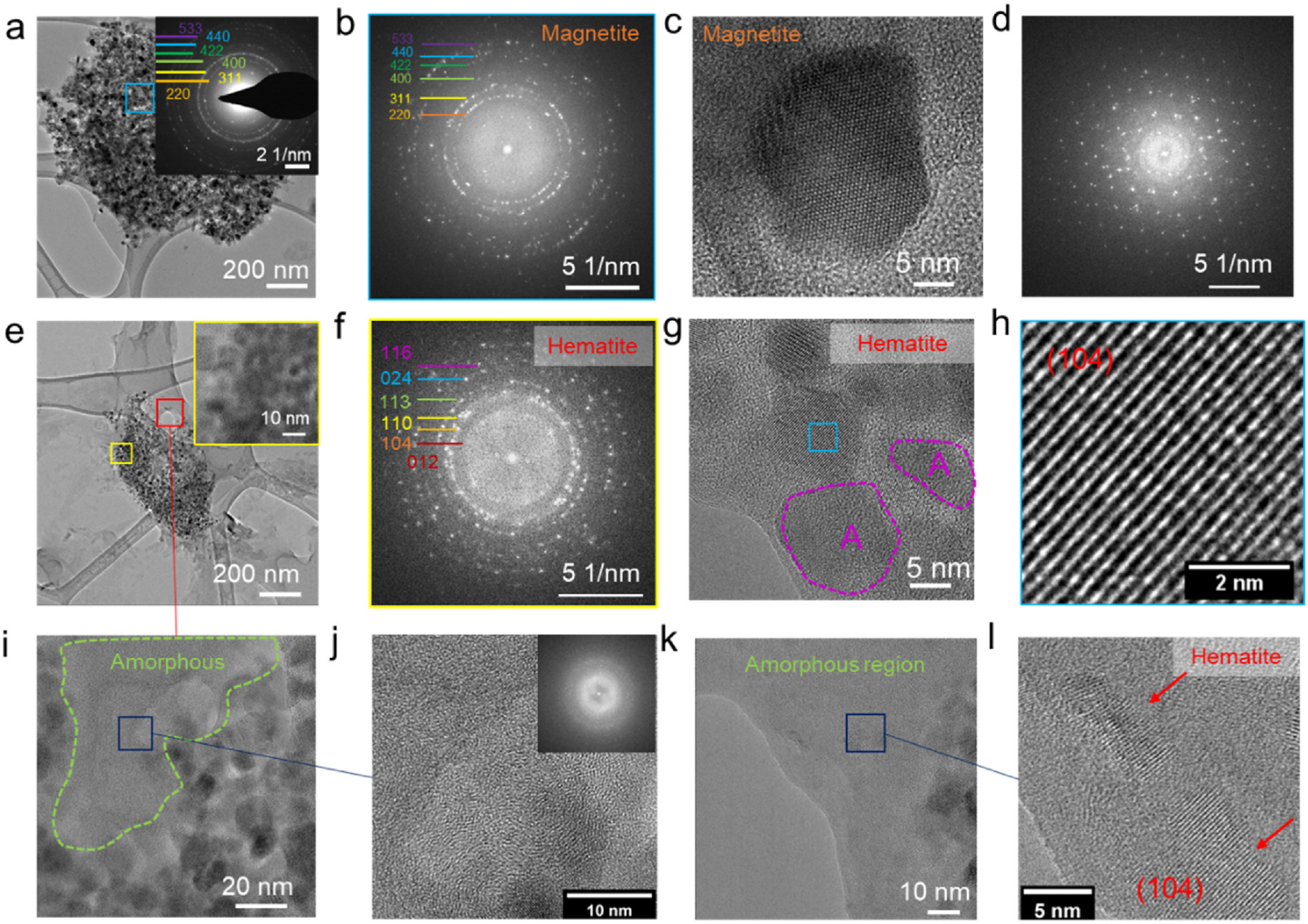

Fig. 3. HRTEM of magnetite nanoparticles after culturing with cyanobacteria. (a) Magnetite nanoparticle aggregates in the substrates without cyanobacteria cultures. Inset: SAED pattern indicates magnetite phase. (b) FFT of sample from the blue box in (a). (c) HRTEM image of a single magnetite nanoparticle in (a). (d) FFT of the nanoparticle is shown in (c). (e) Magnetite nanoparticle aggregates in the substrates with cyanobacteria cultures. Inset: Higher resolution image from (e). (f) FFT of sample from the yellow box in (e), indicating the existence of hematite phase. (g, h) HRTEM of the hematite nanoparticles in (e). (i, j) HRTEM of the regions surrounding the nanoparticle aggregates in (e, red box). Amorphous domains are observed. (k, l) Hematite nanocrystals are noticed in the surrounding amorphous domains. (For interpretation of the references to colour in this figure legend, the reader is referred to the Web version of this article.)

Table 1

Chlorophyll *a* content and siderophore production in G-MTQ-3P2 cyanobacteria cultures in different media after 21 days incubation indicating increased cell numbers in cultures with nanoparticles and no significant differences in iron-depleted medium with or without nanoparticles.

Experiment group	Chlorophyll *a* content (μg/ml)	Siderophore content (μM DFOM equivalents)
Cyanobacteria + iron depleted medium	1.62 ± 0.13	9.4 ± 1.1
Cyanobacteria + iron depleted medium + nanoparticles	3.65 ± 0.20	10.4 ± 1.3
Iron depleted medium	N/A	N/A
Cyanobacteria + iron containing medium	2.01 ± 0.33	4.8 ± 1.3

nanoparticles (Figs. 3k and l). Indeed, abundant extracellular polymeric substances (EPS) have been reported in endolithic communities from arid deserts [3]. EPSs are synthesized by cyanobacteria mainly from sugars, forming a protective shield around cells [62]. EPSs are the principal component of microbial biofilms, they are essential for retaining moisture and nutrients and, with associated organic acids, contribute to mineral weathering [3,63,64]. For example, cyanobacteria, specifically *Chroococcidiopsis*, were shown to trigger the weathering of sandstone by abrupt pH changes as the result of photosynthetic activity [65]. Furthermore, decreases in pH by microbial metabolites were shown to promote iron solubilization under low iron bioavailability. Conversely to the reactions carried out by *Chroococcidiopsis* in this study that lead to dissolution and oxidation to hematite, DIRB organisms such as *Shewanella putrefaciens* have demonstrated reduction reactions that transform iron oxides. A seeming commonality between these systems is the presence of the organic biofilms that surround the mineral and likely play a significant role in solubilization. In fact, multiple studies on bacteria-mineral interactions [18,66–69] revealed direct contact of cells and further hypothesized that extracellular polymers (i.e., exopolysaccharides, EPS) are responsible for the changes to mineral surfaces. The composition of these extracellular polymer substances are currently unknown, and merits a significant future effort in their investigation.

In addition to studying the changes of iron-based mineral nanoparticles, the activities of cyanobacteria cultures were monitored. Because cells and related biological products were difficult to collect on gypsum coupon surfaces, we used liquid culture experiments, in which magnetite nanoparticles were directly added to the culture media. Different sets of experiments were performed, and are shown in Table 1. Chl *a* concentration in the culture, as a proxy for cell abundance, revealed that the samples cultured in low-iron medium with added magnetite nanoparticles had a larger number of cyanobacteria than samples without magnetite (Table 1). The production of siderophores was also higher in the iron-depleted medium compared to the iron-rich medium, suggesting the use siderophores by cyanobacteria to acquire iron from magnetite nanoparticles. However, it is important to note that electron transfer between iron-based mineral and cyanobacteria leading to the phase transformation cannot be ruled out.

3.3. Iron acquisition by cyanobacteria from bulk magnetite crystals

To understand the mineral-microorganisms relation at larger scales, we used cyanobacteria cultured in the presence of bulk magnetite crystals (ca. Those at the millimeter scale). Bulk magnetite crystals were embedded in epoxy and polished to expose the mineral surfaces (Fig. 4a, top). Raman mapping was performed to confirm the original magnetite mineral phase (with almost no hematite) on sample surfaces before the culture experiments (Fig. 4a, bottom). Culture experiments were conducted in both low and high concentrations of soluble iron (Fig. 4b): the upper row consists of 3 samples cultured in iron-depleted media with a limited soluble iron (i.e., samples 1A, 1B, 1C), while the bottom row were samples cultured in regular BG11 media containing iron ions (i.e., samples 2A, 2B, 2C). By conducting this experiment, we aim to determine whether cyanobacteria under iron-limiting conditions could actively acquire iron from a magnetite substrate, causing the dissolution and oxidation of magnetite crystals.

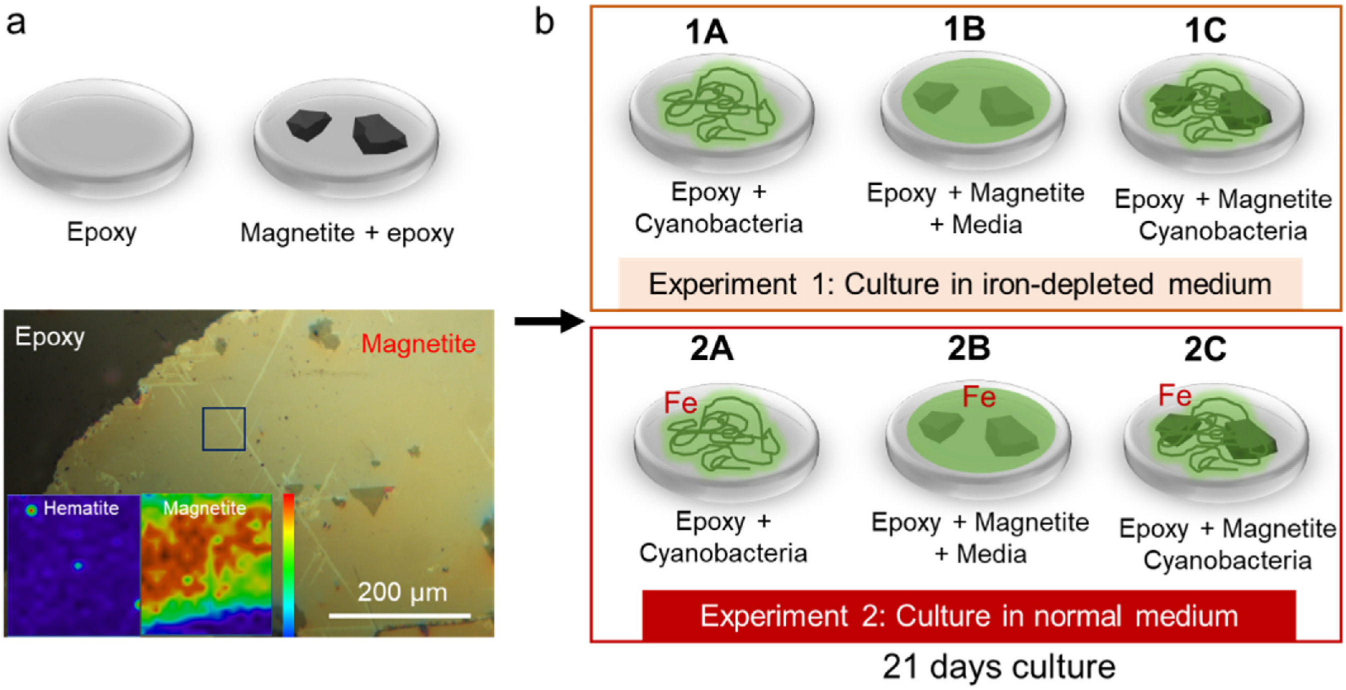

Fig. 4. Experiments of cyanobacteria cultured on large geologic magnetite crystals embedded in epoxy resin. (a) Epoxy coupons with and without large magnetite crystals. Raman mapping verifies the magnetite phase on the substrate (i.e., from large crystals). (b) Two series of different experimental conditions are applied: the upper row are samples (1A, 1B and 1C) cultured in iron-depleted media, while the bottom row are samples (2A, 2B and 2C) cultured in normal media with sufficient concentrations of iron ions. Controls without magnetite and without cyanobacteria were also performed.

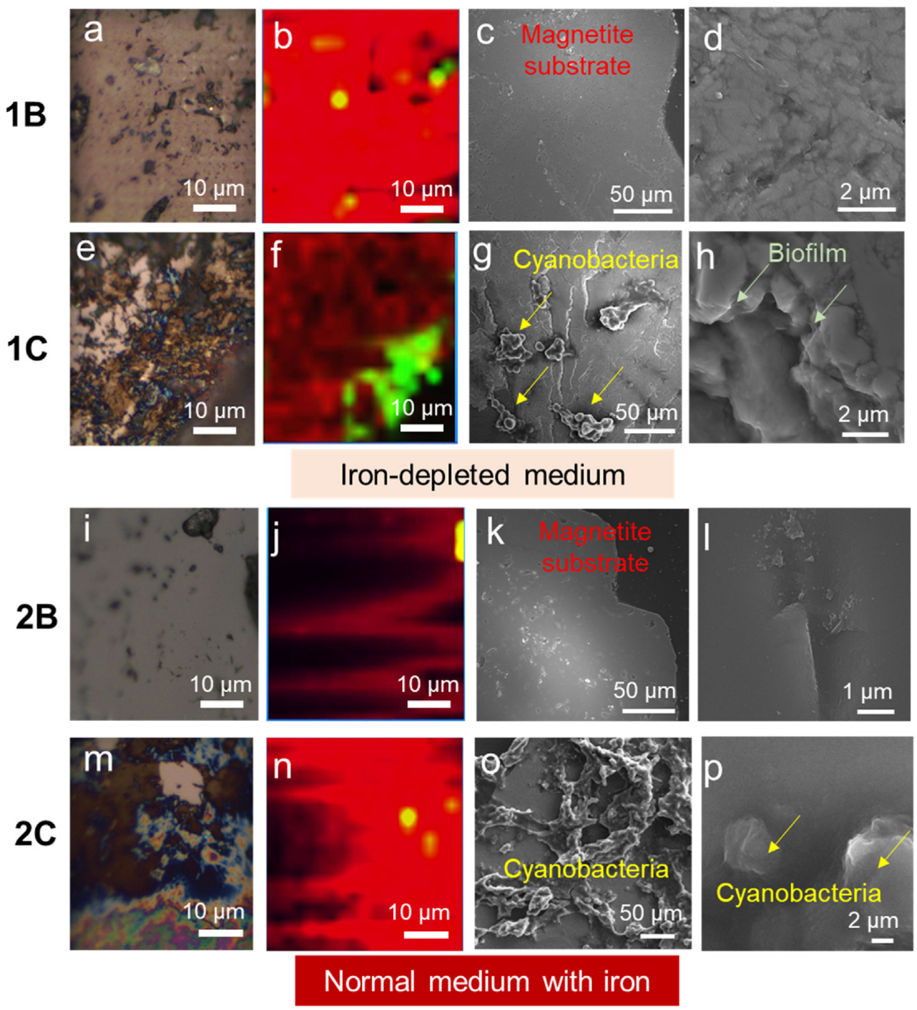

Fig. 5. Interactions between cyanobacteria and magnetite bulk crystals. (a–h) Raman mapping and SEM images of samples cultured in iron-depleted media. The first row (a–d) is the control sample without cyanobacteria culture, corresponding to sample 1B in Fig. 4. The second row (e–h) is the experimental sample of 1C. (a, e) Optical microscopy images of sample surfaces after culturing. (b, f) Raman mapping of control and experimental samples, respectively. (c, d, g and h) SEM images of sample surfaces after cyanobacteria culturing. (i–p) Raman mapping and SEM images of samples cultured in media with sufficient iron ions. The first row (i–l) and second row (m–p) correspond to samples 2B and 2C, respectively, from Fig. 4. In the Raman maps, the red color indicates magnetite phase (Raman shift 666 cm^{-1}), while the green color indicates hematite phase (Raman shift 217 cm^{-1}). A large area of hematite phase is observed in sample 1C. SEM of sample 1C (g, h) and 2C (o, p) show cyanobacteria attaching to the substrate surfaces. Grooves and dissolution of the large magnetite substrate particles are noticed in the SEM images from sample 1C (g, h). (For interpretation of the references to colour in this figure legend, the reader is referred to the Web version of this article.)

Raman spectroscopy and mapping was used to evaluate the different cultured samples (Fig. 5). Note, samples 1A and 2A are not shown as no changes to the epoxy surface were observed. Analysis of the samples cultured in iron-depleted media, reveals that sample 1C (with magnetite and cyanobacteria in iron-depleted media) had a large area of hematite phase (large green area in Figs. 5f and S7) that developed during the culture experiments. SEM images of the same sample (Figs. 5g and h) showed cyanobacteria colonies attached to the surfaces of magnetite crystals. Grooves and cracks were observed on the surface, indicating physical changes likely caused by the dissolution of magnetite when cultured with cyanobacteria (Fig. 5g). Higher magnification imaging in Fig. 5h showed the biofilm on the nanograins of magnetite substrate. However, almost no hematite phase or surface changes were observed in the control sample 1B (magnetite but no cyanobacteria in iron-depleted media, Figs. 5a–d). In contrast, when magnetite substrates were cultured in media with sufficient iron ions (samples 2A-C described from Fig. 4), almost no hematite phase was observed. SEM images from sample 2C (cyanobacteria plus magnetite in normal media), showed that cyanobacteria were attached to the surface of the magnetite substrates. However, the underlying substrate was flat, with no obvious grooves and physical changes observable (Figs. 5o and p). These experimental results indicated that cyanobacteria could acquire iron ions from the bulk magnetite crystals when experiencing iron deficiency (i.e., liquid culture medium in our experiments). Dissolution of nanoparticles and modification of large magnetite crystal surfaces were observed in the presence of biofilms (Figs. 3 and 5). This is likely due to the local low pH of these biofilms, which consist of organic acids that have been shown to etch gypsum rocks [4], and the higher solubility of magnetite in acidic environments [18,70]. This process can be described by the following reaction [71]:

$$\left[Fe_2^{3+}Fe^{2+}\right]O_{4\ (Magnetite)} + 8H^+ \rightarrow Fe^{2+} + 2Fe^{3+} + 4H_2O$$

Furthermore, the use of ferric iron (Fe^{3+}) by the cyanobacteria during photosynthesis and metabolism could drive the reaction forward, leading to additional dissolution. This may also explain observations in sample 2C (Fig. 5), where almost no dissolution of magnetite was observed since there was sufficient iron ions in the culture media, which could impede the dissolution reactions.

In addition, the presence of hematite was observed concurrently with the dissolution of magnetite. Because photosynthetic releases oxygen, components of the reaction can be modified such that: [71]

$$3\left[Fe_2^{3+}Fe^{2+}\right]O_{4\ (Magnetite)} + 2H^+ + 1/20_2 \rightarrow Fe^{2+} + 4\left[Fe_2^{3+}\right]O_{3\ (hematite)} + H_2O$$

Hematite phase is barely observed in sample 2C, further indicating that the magnetite to hematite phase transformation only happened when magnetite dissolution occurred. The oxidation of magnetite to hematite phases was only observed at either high temperatures (>200 °C) or under hydrothermal (>120 °C) conditions [72,73]. We showed here that in presence of metabolically active cyanobacteria, this process could occur under atmospheric pressure and at room temperature. In our experiments, the magnetite to hematite transformation was facilitated by *Chroococcidiopsis*. The higher amount of chlorophyll – a proxy for cell density - we observed in the magnetite nanoparticles containing liquid medium, the changes in nanoparticles size, and the production of siderophores indicated a biological origin for the magnetite to hematite phase transformation.

4. Conclusions and outlook

We identified magnetite and hematite phases in the gypsum rocks collected from the Atacama Desert. Microorganisms were clustered on or near the iron oxide minerals occluded within these rocks, indicating these inorganic minerals may be used as an iron source in this extreme environment. A previously isolated *Chroococcidiopsis* strain was cultured with synthesized magnetite nanoparticles. Shrinkage of nanoparticle size and the concurrent emergence of amorphous domains surrounding the nanocrystals indicated a process of magnetite dissolution in presence of the cyanobacterial biofilm. The production of EPSs in embedded magnetite nanoparticles and siderophores in a liquid medium supplemented with magnetite nanoparticles further suggest that cyanobacteria were able to extract iron from the magnetite solid phase. The dissolution of solid magnetite phase was further verified in large bulk magnetite crystals, revealing phase transformation from magnetite to hematite during culture experiments, most likely as the result of oxygen production by photosynthesis. These experiments demonstrated that magnetite minerals can be used as an iron source by cyanobacteria in culture experiments and may similarly enable the survival of microorganisms living in extreme environments. To understand this process thoroughly, future work will involve additional *in-situ* analyses to monitor and understand the interactions between living cells and inorganic minerals in real-time. The oxidation of magnetite to hematite at room temperature by living organisms could provide potential design strategies for engineered living materials. Thus, smart and intelligent materials that react to environmental stimuli can be made by incorporating living microorganisms in fabrication processes such as additive manufacturing.

Credit author statement

Wei Huang: Conceptualization, Methodology, Formal analysis, Investigation, Visualization, Writing – original draft, Writing – review & editing. **Taifeng Wang:** Formal analysis, Visualization, Investigation. **Cesar Perez-Fernandez:** Formal analysis, Visualization, Investigation. **Jocelyne DiRuggiero:** Conceptualization, Methodology, Formal analysis, Writing – original draft, Writing – review & editing, Funding acquisition. **David Kisailus:** Conceptualization, Methodology, Formal analysis, Visualization, Writing – original draft, Writing - review & editing, Supervision, Project administration, Funding acquisition.

Declaration of competing interest

The authors declare that they have no known competing financial interests or personal relationships that could have appeared to influence the work reported in this paper.

Data availability

Data will be made available on request.

Acknowledgements

This work was supported by the Army Research Office, Microbiology Program (W911NF-18-1-0253) and Biochemistry Program (W911NF-20-1-0201). We thank Dr. Sirine Fakra at the Lawrence Berkeley National Lab for the help of conducting the synchrotron micro-XRF and XANES experiments. This research used resources of the Advanced Light Source, a U.S. DOE Office of Science User Facility under contract no. DE-AC02-05CH11231s.

Appendix A. Supplementary data

Supplementary data to this article can be found online at https://doi.org/10.1016/j.mtbio.2022.100493.

References

[1] D. Schulze-Makuch, D. Wagner, S.P. Kounaves, K. Mangelsdorf, K.G. Devine, J.-P. de Vera, P. Schmitt-Kopplin, H.-P. Grossart, V. Parro, M. Kaupenjohann, Transitory microbial habitat in the hyperarid Atacama Desert, Proc. Natl. Acad. Sci. USA 115 (11) (2018) 2670–2675.

[2] J. Wierzchos, C. Ascaso, C.P. McKay, Endolithic cyanobacteria in halite rocks from the hyperarid core of the Atacama Desert, Astrobiology 6 (3) (2006) 415–422.

[3] P.H. Lebre, P. De Maayer, D.A. Cowan, Xerotolerant bacteria: surviving through a dry spell, Nat. Rev. Microbiol. 15 (5) (2017) 285–296.

[4] W. Huang, E. Ertekin, T. Wang, L. Cruz, M. Dailey, J. DiRuggiero, D. Kisailus, Mechanism of water extraction from gypsum rock by desert colonizing microorganisms, Proc. Natl. Acad. Sci. USA 117 (20) (2020) 10681–10687.

[5] J.J. Walker, N.R. Pace, Endolithic microbial ecosystems, Annu. Rev. Microbiol. 61 (2007) 331–347.

[6] E.B. Qu, C.R. Omelon, A. Oren, V. Meslier, D.A. Cowan, G. Maggs-Kölling, J. DiRuggiero, Trophic selective pressures organize the composition of endolithic microbial communities from global deserts, Front. Microbiol. 10 (2020) 2952.

[7] J. Nogales, S. Gudmundsson, E.M. Knight, B.O. Palsson, I. Thiele, Detailing the optimality of photosynthesis in cyanobacteria through systems biology analysis, Proc. Natl. Acad. Sci. USA 109 (7) (2012) 2678–2683.

[8] C. Kranzler, M. Rudolf, N. Keren, E. Schleiff, Iron in cyanobacteria, Adv. Bot. Res. 65 (2013) 57–105.

[9] R.M. Hazen, S.M. Morrison, On the paragenetic modes of minerals: a mineral evolution perspective, Am. Mineral. 107 (7) (2022) 1262–1287.

[10] J. Kramer, Ö. Özkaya, R. Kümmerli, Bacterial siderophores in community and host interactions, Nat. Rev. Microbiol. 18 (3) (2020) 152–163.

[11] L. Shi, H. Dong, G. Reguera, H. Beyenal, A. Lu, J. Liu, H.-Q. Yu, J.K. Fredrickson, Extracellular electron transfer mechanisms between microorganisms and minerals, Nat. Rev. Microbiol. 14 (10) (2016) 651–662.

[12] C. Wandersman, P. Delepelaire, Bacterial iron sources: from siderophores to hemophores, Annu. Rev. Microbiol. 58 (2004) 611–647.

[13] S.W. Wilhelm, C.G. Trick, Iron-limited growth of cyanobacteria: multiple siderophore production is a common response, Limnol. Oceanogr. 39 (8) (1994) 1979–1984.

[14] G.-W. Qiu, C. Koedooder, B.-S. Qiu, Y. Shaked, N. Keren, Iron transport in cyanobacteria–from molecules to communities, Trends Microbiol. 30 (3) (2022).

[15] H. Yu, J.R. Leadbetter, Bacterial chemolithoautotrophy via manganese oxidation, Nature 583 (7816) (2020) 453–458.

[16] F. Crundwell, How do bacteria interact with minerals? Hydrometallurgy 71 (1–2) (2003) 75–81.

[17] H. Dong, J.K. Fredrickson, D.W. Kennedy, J.M. Zachara, R.K. Kukkadapu, T.C. Onstott, Mineral transformations associated with the microbial reduction of magnetite, Chem. Geol. 169 (3–4) (2000) 299–318.

[18] J.E. Kostka, K.H. Nealson, Dissolution and reduction of magnetite by bacteria, Environ. Sci. Technol. 29 (10) (1995) 2535–2540.

[19] D.R. Lovley, M.J. Baedecker, D.J. Lonergan, I.M. Cozzarelli, E.J. Phillips, D.I. Siegel, Oxidation of aromatic contaminants coupled to microbial iron reduction, Nature 339 (6222) (1989) 297–300.

[20] K.H. Nealson, D. Saffarini, Iron and manganese in anaerobic respiration: environmental significance, physiology, and regulation, Annu. Rev. Microbiol. 48 (1994) 311–344.

[21] K. Arai, S. Murata, T. Wang, W. Yoshimura, M. Oda-Tokuhisa, T. Matsunaga, D. Kisailus, A. Arakaki, Adsorption of biomineralization protein Mms6 on magnetite (Fe_3O_4) nanoparticles, Int. J. Mol. Sci. 23 (10) (2022) 5554.

[22] T. Wang, W. Huang, C.H. Pham, S. Murata, S. Herrera, N.D. Kirchhofer, B. Arkook, D. Stekovic, M.E. Itkis, N. Goldman, L. Zepeda-Ruiz, M. Zhernenkov, M. Nemoto, A. Arakaki, D. Kisailus, Mesocrystalline ordering and phase transformation of iron oxide biominerals in the ultrahard teeth of Cryptochiton stelleri, Small Structures 3 (4) (2022), 2100202.

[23] M. Nemoto, D. Ren, S. Herrera, S. Pan, T. Tamura, K. Inagaki, D. Kisailus, Integrated transcriptomic and proteomic analyses of a molecular mechanism of radular teeth biomineralization in Cryptochiton stelleri, Sci. Rep. 9 (1) (2019) 1–10.

[24] A. Arakaki, A. Yamagishi, A. Fukuyo, M. Tanaka, T. Matsunaga, Co-ordinated functions of Mms proteins define the surface structure of cubo-octahedral magnetite crystals in magnetotactic bacteria, Mol. Microbiol. 93 (3) (2014) 554–567.

[25] Q. Wang, M. Nemoto, D. Li, J.C. Weaver, B. Weden, J. Stegemeier, K.N. Bozhilov, L.R. Wood, G.W. Milliron, C.S. Kim, E. DiMasi, D. Kisailus, Phase transformations and structural developments in the radular teeth of Cryptochiton stelleri, Adv. Funct. Mater. 23 (23) (2013) 2908–2917.

[26] M. Nemoto, Q. Wang, D. Li, S. Pan, T. Matsunaga, D. Kisailus, Proteomic analysis from the mineralized radular teeth of the giant Pacific chiton, Cryptochiton stelleri (Mollusca), Proteomics 12 (18) (2012) 2890–2894.

[27] J.C. Weaver, Q. Wang, A. Miserez, A. Tantuccio, R. Stromberg, K.N. Bozhilov, P. Maxwell, R. Nay, S.T. Heier, E. DiMasi, D. Kisailus, Analysis of an ultra hard magnetic biomineral in chiton radular teeth, Mater. Today 13 (1–2) (2010) 42–52.

[28] A. Arakaki, J. Webb, T. Matsunaga, A novel protein tightly bound to bacterial magnetic particles in Magnetospirillum magneticum strain AMB-1, J. Biol. Chem. 278 (10) (2003) 8745–8750.

[29] T. Matsunaga, T. Sakaguchi, F. Tadakoro, Magnetite formation by a magnetic bacterium capable of growing aerobically, Appl. Microbiol. Biotechnol. 35 (5) (1991) 651–655.

[30] K. McNamara, S.A. Tofail, Nanosystems: the use of nanoalloys, metallic, bimetallic, and magnetic nanoparticles in biomedical applications, Phys. Chem. Chem. Phys. 17 (42) (2015) 27981–27995.

[31] K. McNamara, S.A. Tofail, Nanoparticles in biomedical applications, Adv. Phys. X 2 (1) (2017) 54–88.

[32] Y.-T. Chen, A.G. Kolhatkar, O. Zenasni, S. Xu, T.R. Lee, Biosensing using magnetic particle detection techniques, Sensors 17 (10) (2017) 2300.

[33] Y. Chen, X. Ding, Y. Zhang, A. Natalia, X. Sun, Z. Wang, H. Shao, Design and synthesis of magnetic nanoparticles for biomedical diagnostics, Quant. Imag. Med. Surg. 8 (9) (2018) 957.

[34] L.S. Ganapathe, M.A. Mohamed, R. Mohamad Yunus, D.D. Berhanuddin, Magnetite (Fe_3O_4) nanoparticles in biomedical application: from synthesis to surface functionalisation, Magnetochemistry 6 (4) (2020) 68.

[35] G. Liu, J. Gao, H. Ai, X. Chen, Applications and potential toxicity of magnetic iron oxide nanoparticles, Small 9 (9–10) (2013) 1533–1545.

[36] E. Ozawa, Microwave-assisted magnetization reversal in dispersed nanosized barium ferrite particles for high-density magnetic recording tape, IEEE Trans. Magn. 55 (7) (2019) 1–4.

[37] H.-w. Zhang, Y. Liu, S.-h. Sun, Synthesis and assembly of magnetic nanoparticles for information and energy storage applications, Front. Phys. China 5 (4) (2010) 347–356.

[38] S. Kyle, 3D printing of bacteria: the next frontier in biofabrication, Trends Biotechnol. 36 (4) (2018) 340–341.

[39] M. Schaffner, P.A. Rühs, F. Coulter, S. Kilcher, A.R. Studart, 3D printing of bacteria into functional complex materials, Sci. Adv. 3 (12) (2017), eaao6804.

[40] A. Xin, Y. Su, S. Feng, M. Yan, K. Yu, Z. Feng, K. Hoon Lee, L. Sun, Q. Wang, Growing living composites with ordered microstructures and exceptional mechanical properties, Adv. Mater. 33 (13) (2021), 2006946.

[41] A. Rodrigo-Navarro, S. Sankaran, M.J. Dalby, A. del Campo, M. Salmeron-Sanchez, Engineered living biomaterials, Nat. Rev. Mater. (2021) 1–16.

[42] C.M. Heveran, S.L. Williams, J. Qiu, J. Artier, M.H. Hubler, S.M. Cook, J.C. Cameron, W.V. Srubar III, Biomineralization and successive regeneration of engineered living building materials, Matter 2 (2) (2020) 481–494.

[43] P.Q. Nguyen, N.M.D. Courchesne, A. Duraj-Thatte, P. Praveschotinunt, N.S. Joshi, Engineered living materials: prospects and challenges for using biological systems to direct the assembly of smart materials, Adv. Mater. 30 (19) (2018), 1704847.

[44] W. Ma, A. Saccardo, D. Roccatano, D. Aboagye-Mensah, M. Alkaseem, M. Jewkes, F. Di Nezza, M. Baron, M. Soloviev, E. Ferrari, Modular assembly of proteins on nanoparticles, Nat. Commun. 9 (1) (2018) 1–9.

[45] C. Debus, B. Wu, T. Kollmann, P. Duchstein, M. Siglreitmeier, S. Herrera, D. Benke, D. Kisailus, D. Schwahn, V. Pipich, D. Faivre, D. Zahn, H. Colfen, Bioinspired multifunctional layered magnetic hybrid materials, Bioinspired, Biomimetic Nanobiomaterials 8 (1) (2019) 28–46.

[46] J.M. Johnson, N. Kinsinger, C. Sun, D. Li, D. Kisailus, Urease-mediated room-temperature synthesis of nanocrystalline titanium dioxide, J. Am. Chem. Soc. 134 (34) (2012) 13974–13977.

[47] P. Curnow, D. Kisailus, D.E. Morse, Biocatalytic synthesis of poly (l-Lactide) by native and recombinant forms of the silicatein enzymes, Angew. Chem. 118 (4) (2006) 629–632.

[48] P. Curnow, P.H. Bessette, D. Kisailus, M.M. Murr, P.S. Daugherty, D.E. Morse, Enzymatic synthesis of layered titanium phosphates at low temperature and neutral pH by cell-surface display of silicatein-α, J. Am. Chem. Soc. 127 (45) (2005) 15749–15755.

[49] D. Kisailus, J.H. Choi, J.C. Weaver, W. Yang, D.E. Morse, Enzymatic synthesis and nanostructural control of gallium oxide at low temperature, Adv. Mater. 17 (3) (2005) 314–318.

[50] J.L. Sumerel, W. Yang, D. Kisailus, J.C. Weaver, J.H. Choi, D.E. Morse, Biocatalytically templated synthesis of titanium dioxide, Chem. Mater. 15 (25) (2003) 4804–4809.

[51] H. Ehrlich, E. Bailey, M. Wysokowski, T. Jesionowski, Forced biomineralization: a review, Biomimetics 6 (3) (2021) 46.

[52] H. Ehrlich, M. Wysokowski, T. Jesionowski, The Philosophy of Extreme Biomimetics, Sustainable Materials and Technologies, 2022, e00447.

[53] B. Murray, M. Dailey, E. Ertekin, J. DiRuggiero, F.J. Stewart, Draft metagenomes of endolithic cyanobacteria and cohabitants from hyper-arid deserts, Microbiology Resource Announcements 10 (30) (2021) e00206–e00221.

[54] C.D. Cox, Deferration of laboratory media and assays for ferric and ferrous ions, Methods Enzymol. 235 (1994) 315–329.

[55] T. Zavřel, M.A. Sinetova, J. Červený, Measurement of chlorophyll a and carotenoids concentration in cyanobacteria, Bio-protocol 5 (9) (2015) e1467.

[56] D. Alexander, D. Zuberer, Use of chrome azurol S reagents to evaluate siderophore production by rhizosphere bacteria, Biol. Fertil. Soils 12 (1) (1991) 39–45.

[57] J. Wierzchos, J. DiRuggiero, P. Vítek, O. Artieda, V. Souza-Egipsy, P. Skaloud, M. Tisza, A.F. Davila, C. Vílchez, I. Garbayo, Adaptation strategies of endolithic chlorophototrophs to survive the hyperarid and extreme solar radiation environment of the Atacama Desert, Front. Microbiol. 6 (2015) 934.

[58] E. Ertekin, V. Meslier, A. Browning, J. Treadgold, J. DiRuggiero, Rock structure drives the taxonomic and functional diversity of endolithic microbial communities in extreme environments, Environ. Microbiol. 23 (7) (2021) 3937–3956.

[59] V. Meslier, M.C. Casero, M. Dailey, J. Wierzchos, C. Ascaso, O. Artieda, P. McCullough, J. DiRuggiero, Fundamental drivers for endolithic microbial community assemblies in the hyperarid Atacama Desert, Environ. Microbiol. 20 (5) (2018) 1765–1781.

[60] D. Bersani, P. Lottici, A. Montenero, Micro-Raman investigation of iron oxide films and powders produced by sol–gel syntheses, J. Raman Spectrosc. 30 (5) (1999) 355–360.

[61] A. Rygula, K. Majzner, K.M. Marzec, A. Kaczor, M. Pilarczyk, M. Baranska, Raman spectroscopy of proteins: a review, J. Raman Spectrosc. 44 (8) (2013) 1061–1076.

[62] G. Mazor, G.J. Kidron, A. Vonshak, A. Abeliovich, The role of cyanobacterial exopolysaccharides in structuring desert microbial crusts, FEMS (Fed. Eur. Microbiol. Soc.) Microbiol. Ecol. 21 (2) (1996) 121–130.

[63] C. Balland, A. Poszwa, C. Leyval, C. Mustin, Dissolution rates of phyllosilicates as a function of bacterial metabolic diversity, Geochem. Cosmochim. Acta 74 (19) (2010) 5478–5493.

[64] N. Mergelov, C.W. Mueller, I. Prater, I. Shorkunov, A. Dolgikh, E. Zazovskaya, V. Shishkov, V. Krupskaya, K. Abrosimov, A. Cherkinsky, Alteration of rocks by endolithic organisms is one of the pathways for the beginning of soils on Earth, Sci. Rep. 8 (1) (2018) 1–15.

[65] B. Büdel, B. Weber, M. Kühl, H. Pfanz, D. Sültemeyer, D. Wessels, Reshaping of sandstone surfaces by cryptoendolithic cyanobacteria: bioalkalization causes chemical weathering in arid landscapes, Geobiology 2 (4) (2004) 261–268.

[66] K.H. Nealson, B. Little, Breathing manganese and iron: solid-state respiration, Adv. Appl. Microbiol. 45 (1997) 213–239.

[67] C.O. Obuekwe, D.W. Westlake, F.D. Cook, J. William Costerton, Surface changes in mild steel coupons from the action of corrosion-causing bacteria, Appl. Environ. Microbiol. 41 (3) (1981) 766–774.

[68] R.G. Arnold, T.J. DiChristina, M.R. Hoffmann, Reductive dissolution of Fe (III) oxides by Pseudomonas sp, 200, Biotechnology and Bioengineering 32 (9) (1988) 1081–1096.

[69] J.K. Fredrickson, J.M. Zachara, D.W. Kennedy, H. Dong, T.C. Onstott, N.W. Hinman, S.-m. Li, Biogenic iron mineralization accompanying the dissimilatory reduction of hydrous ferric oxide by a groundwater bacterium, Geochem. Cosmochim. Acta 62 (19–20) (1998) 3239–3257.

[70] R. Salmimies, M. Mannila, J. Juha, A. Häkkinen, Acidic dissolution of magnetite: experimental study on the effects of acid concentration and temperature, Clays Clay Miner. 59 (2) (2011) 136–146.

[71] A.F. White, M.L. Peterson, M.F. Hochella Jr., Electrochemistry and dissolution kinetics of magnetite and ilmenite, Geochem. Cosmochim. Acta 58 (8) (1994) 1859–1875.

[72] S. Nasrazadani, A. Raman, The application of infrared spectroscopy to the study of rust systems—II. Study of cation deficiency in magnetite (Fe_3O_4) produced during its transformation to maghemite (γ-Fe_2O_3) and hematite (α-Fe_2O_3), Corrosion Sci. 34 (8) (1993) 1355–1365.

[73] Z. Li, C. Chanéac, G. Berger, S. Delaunay, A. Graff, G. Lefèvre, Mechanism and kinetics of magnetite oxidation under hydrothermal conditions, RSC Adv. 9 (58) (2019) 33633–33642.